



Published in final edited form as:

Neuroimage. 2019 January 15; 185: 685–698. doi:10.1016/j.neuroimage.2018.06.069.

Age-specific gray and white matter DTI atlas for human brain at 33, 36 and 39 postmenstrual weeks

Lei Feng^{#1,2}, Hang Li^{#1,3}, Kenichi Oishi⁴, Virendra Mishra⁵, Limei Song^{1,2}, Qinmu Peng^{1,6}, Minhui Ouyang^{1,5}, Jiaojian Wang^{1,6}, Michelle Slinger¹, Tina Jeon¹, Lizette Lee⁷, Roy Heyne⁷, Lina Chalakh⁷, Yun Peng³, Shuwei Liu², and Hao Huang^{1,5,6,*}

¹Department of Radiology, Children's Hospital of Philadelphia, PA, USA

²Research Center for Sectional and Imaging Anatomy, Shandong University Cheeloo College of Medicine, Shandong, China

³Department of Radiology, Beijing Children's Hospital Affiliated to Capital Medical University, Beijing, China

⁴Department of Radiology, Johns Hopkins University, MD, USA

⁵Advanced Imaging Research Center, University of Texas Southwestern Medical Center, TX, USA

⁶Department of Radiology, Perelman School of Medicine, University of Pennsylvania, PA, USA

⁷Department of Pediatrics, University of Texas Southwestern Medical Center, TX, USA

These authors contributed equally to this work.

Abstract

During the 3rd trimester, dramatic structural changes take place in the human brain, underlying the neural circuit formation. The survival rate of premature infants has increased significantly in recent years. The large morphological differences of the preterm brain at 33 or 36 postmenstrual weeks (PMW) from the brain at 40PMW (full term) make it necessary to establish age-specific atlases for preterm brains. In this study, with high quality (1.5×1.5×1.6mm³ imaging resolution) diffusion tensor imaging (DTI) data obtained from 84 healthy preterm and term-born neonates, we established age-specific preterm and term-born brain templates and atlases at 33, 36 and 39PMW. Age-specific DTI templates include a single-subject template, a population-averaged template with linear transformation and a population-averaged template with nonlinear transformation. Each of the age-specific DTI atlases includes comprehensive labeling of 126 major gray matter (GM) and white matter (WM) structures, specifically 52 cerebral cortical structures, 40 cerebral WM structures, 22 brainstem and cerebellar structures and 12 subcortical GM structures. From 33 to 39 PMW, dramatic morphological changes of delineated individual neural structures such as ganglionic eminence and uncinat fasciculus were revealed. The evaluation based on

*Corresponding Author: Hao Huang, Ph.D., 3401 Civic Center Blvd, Philadelphia, PA 19104; huangh6@email.chop.edu, Tel: 267-426-5701; Fax: 215-590-1345.

Publisher's Disclaimer: This is a PDF file of an unedited manuscript that has been accepted for publication. As a service to our customers we are providing this early version of the manuscript. The manuscript will undergo copyediting, typesetting, and review of the resulting proof before it is published in its final citable form. Please note that during the production process errors may be discovered which could affect the content, and all legal disclaimers that apply to the journal pertain.

measurements of Dice ratio and L1 error suggested reliable and reproducible automated labels from the age-matched atlases compared to labels from manual delineation. Applying these atlases to automatically and effectively delineate microstructural changes of major WM tracts during the 3rd trimester was demonstrated. The established age-specific DTI templates and atlases of 33, 36 and 39 PMW brains may be used for not only understanding the complicated yet precisely organized functional and structural maturational processes but also detecting neural disorder biomarkers of the preterm brains as clinical references.

Keywords

age-specific; atlas; template; preterm; neonate; DTI; comprehensive labels; biomarker

1. Introduction

With the advances in critical care of preterm infants, the survival rate of premature infants has increased significantly in recent years. Identifying abnormalities in the early phase of injuries and understanding injury development are becoming more important than ever. Preterm neonates are a vulnerable population and could suffer from negative neurodevelopmental outcome (e.g. Woodward et al., 2006) or other concurrent morbidities (e.g. Wilson-Costello et al., 2005). The imaging of preterm or term-born infants for clinical indications is of great interest. Routinely used diagnostic methods, such as electronic monitoring and ultrasound, often have poor sensitivity to the abnormalities in neonate brains. Furthermore, it has been demonstrated that various injuries, due to perinatal risks, often lead to damage in selective white matter (WM) (e.g. Huppi et al., 1998; Huppi et al., 2001; Huppi and Inder, 2001; Neil et al., 2002; Rutherford et al, 2004). Age-specific preterm brain atlases that include comprehensive neuroanatomical information of gray matter (GM) structures and WM tracts for precisely delineating anatomical abnormalities are urgently needed.

During the 3rd trimester of brain development, complicated yet precisely organized molecular and cellular processes take place in the human brain, resulting in significant neuroanatomical changes of almost all brain structures. These processes include cell proliferation, neuronal migration, synapse formation and myelination (Sidman and Rakic., 1973; Kostovic and Jovanov-Milosevic, 2006; Bystron et al., 2008). The rapid brain developmental processes also make this period a vulnerable one for potential neurodevelopmental disorders. Comprehensive adult brain atlases (e.g. Mori et al., 2008; Oishi et al., 2008; Thiebaut de Schotten et al., 2011) are relatively well established and have become effective clinical references. However, despite rapid morphological changes of preterm brains, age-specific atlases for preterm neonates at different developmental stages are scarce. The preterm period is critical for understanding the brain circuit formation and network reconfiguration (e.g. Doria et al, 2010; Ball et al., 2014; Cao et al., 2017). Establishing the age-specific neuroanatomical account for comprehensive GM and WM neural structures is imperative for not only offering much needed clinical references but also understanding the brain circuit maturation during the preterm development. There are many transient structures which are unique in this developmental stage and disappear at term or

during childhood development. These unique structures can be found in both WM and the cerebral wall, and are usually associated with specific neurodevelopment processes. For example, ganglionic eminence (GE) (Bayer and Altman, 2004; Huang et al., 2006 and 2009) exists in the human fetal and preterm brain, but disappears at normal time of birth. Some other neural structures, such as superior longitudinal fasciculus, exist in the adult human brain but are almost absent in early preterm brains. Age-specific preterm brain atlas with rich anatomical information can bring us insight into the developmental pattern of individual brain structures.

Diffusion tensor imaging (DTI) (Basser et al., 1994), a type of magnetic resonance imaging (MRI) method, is an effective noninvasive approach for delineating various neuroanatomical structures in the human brain. DTI-derived maps, including fractional anisotropy (FA) map (Pierpaoli and Basser, 1996; Beaulieu, 2002), orientation-encoded colormap (OEC) (Pajevic and Pierpaoli, 1999), axial, radial and mean diffusivity (AD, RD and MD), offer high contrasts of brain tissues. DTI is a uniquely suitable approach for delineating various neuroanatomical structures in the preterm and fetal brain. The emergence and maturation of individual WM tracts have been revealed with DTI-based tractography from as early as the beginning of the 2nd trimester to birth (e.g. Dubois et al., 2006; Huang et al., 2006; Huang et al., 2009, Huang, 2010; Vasung et al., 2010; Oishi et al., 2011; Takahashi et al., 2011; Huang and Vasung, 2014; Ouyang et al., 2015). With relatively high FA in immature cerebral cortex (e.g. McKinstry et al. 2002; Huang et al., 2013; Yu et al., 2016), the morphological maturation of the fetal and preterm cerebral cortex can also be well delineated with DTI. So far, a comprehensive DTI atlas (Oishi et al., 2011) is only available for term-born neonates. Age-specific preterm brain templates (e.g. Kuklisova-Murgasova et al., 2011) have been recently established, but are based on T2-weighted MRI, not DTI. In addition, there are no specific neural structural labels in these preterm brain templates.

In this study, we aimed to establish not only age-specific population-averaged preterm brain DTI templates, but also age-specific preterm brain DTI atlases with comprehensive GM and WM labels. Postmenstrual weeks (PMW) based on the policy statement by American Academy of Pediatrics Committee (Engle et al., 2004) was used here for describing the preterm brain ages. The DTI atlases and templates were established from the high resolution DTI datasets ($1.5 \times 1.5 \times 1.6 \text{mm}^3$ imaging resolution) of 84 healthy preterm and term-born neonates. Single-subject (SS), population-averaged-linear, population-average-nonlinear DTI templates at 33, 36 and 39PMW were established. DTI atlases at 33, 36 and 39PMW were also generated with each including 126 comprehensive GM and WM labels appearing smooth in all axial, coronal and sagittal planes. All presented atlases and templates will be disseminated through the public website brainmrimap.org. The dramatic local volume changes among the brains at these three time points were quantified and illustrated, confirming the importance of establishing age-specific preterm brain atlases and templates. We also tested the reliability and accuracy of potential application of these age-specific atlases for automated labeling. Application of these age-specific DTI atlases to study WM tract microstructural maturation during the 3rd trimester was demonstrated.

2. Materials and Methods

2.1 Preterm and term-born neonate subjects

All the neonates were recruited from Parkland Hospital and scanned at Children's Medical Center at Dallas. 107 normal preterm and term neonates were consented, of which 89 neonates were scanned at the age of 31 to 42 postmenstrual weeks (PMW) and 84 were included in the study. The included neonates were part of the cohort for studying normal prenatal and perinatal development. They were selected after rigorous screening procedures conducted by an experienced neonatologist and an experienced pediatric neuroradiologist, based on subjects' ultrasound, clinical MRI, and subjects' and mothers' medical record. The exclusion criteria include the mother's excessive drug or alcohol abuse during pregnancy; periventricular leukomalacia; hypoxic-ischemic encephalopathy; Grade III-IV intraventricular hemorrhage; body or heart malformations; chromosomal abnormalities, lung disease or bronchopulmonary dysplasia; necrotizing enterocolitis requiring intestinal resection or complex feeding/nutritional disorders; defects or anomalies of the brain; brain tissue dysplasia or hypoplasia; abnormal meninges; alterations in the pial or ventricular surface; or WM lesions. As shown in the histogram of Figure 1 with age and gender distribution of all included 84 subjects, these subjects were divided into 3 age groups as follows: 17 preterm neonates scanned at 31.86 to 34.57 PMW, 34 preterm neonates scanned at 34.57 to 37.57 PMW and 33 term neonates scanned at 37.57 to 41.71 PMW were categorized into age group of 33PMW, 36PMW and 39PMW, respectively. The three age groups were used to keep the sample size in each group large enough to differentiate the structural differences between the adjacent age groups (see power analysis in Supplemental Table 1), given ages of neonates in acquired datasets shown in Figure 1. The Institutional Review Board (IRB) at the University of Texas Southwestern Medical Center approved the study. All subjects' parents gave informed written consent approved by the IRB.

2.2 Acquisition of neonate diffusion MRI and postprocessing

All MRI scans of the neonates were performed during their natural sleep without sedation. All neonates were well fed before the scan. Besides earplugs and earphones, extra foam padding was applied to reduce the sound of the scanner to ensure neonates asleep during the scan. Diffusion MRI (dMRI) was acquired from a 3T Philips Achieva MR system (Philips Healthcare, Best, The Netherlands). The dMRI imaging parameters were as follows: TE=78 ms, TR=6850 ms, in-plane field of view= 168×168 mm², in-plane imaging resolution=1.5×1.5 mm², slice thickness=1.6 mm, slice number=60, 30 independent diffusion encoding directions, b = 1000s/mm², and repetition=2. The total scanning time for dMRI was 11 min. With 30 diffusion weighted image (DWI) volumes and 2 repetitions, only the dMRI datasets with less than 5 volumes affected by motion were accepted. The affected volumes were replaced by the good volumes of another dMRI repetition during postprocessing. DMRI acquired from all the subjects was processed offline using DTIStudio (mrstudio.org). All DWIs was registered to the b0 image using a 12-parameter affine transformation for correction of motion and distortion caused by eddy currents. Diffusion tensor fitting was conducted with corrected DWIs. DTI-derived FA maps, MD, AD and RD maps were obtained for all subjects after tensor fitting. DTI OEC maps indicating fiber orientation were also obtained with red (R), green (G), and blue (B) colors assigned to left-

right, anterior-posterior, and superior-inferior orientations, respectively. All DTI-derived maps were then resliced to 0.6 mm isotropic resolution with $180 \times 220 \times 180$ matrix to establish the templates and atlases below.

2.3 Establishment of age-specific single-subject and population-averaged DTI templates

For each specific age of 33, 36 and 39PMW, two population-averaged templates and a single-subject template were established. The two population-averaged templates included a population-averaged-linear (from linear transformation) and a population-averaged-nonlinear (from nonlinear transformation) template. To generate these age-specific DTI templates at 33, 36 and 39PMW, the six-step procedures used for establishing the JHU neonate atlas (Oishi et al., 2011) were adopted. Briefly, these 6 steps include one step of anterior commissure-posterior commissure (AC-PC) alignment, one step of direct averaging of images, three consecutive steps of averaging of images after three affine transformations respectively and one last step of averaging after dualchannel large deformation diffeomorphic metric mapping (LDDMM) transformation (Miller et al., 2002; Ceritoglu et al., 2009). In the last step of dual-channel LDDMM, both FA and MD maps were used to drive the transformations. The population-averaged-linear and population-average-nonlinear templates are the outcome of the 4th and 6th step, respectively. A single-subject image with the brain shape best matching that of the age-specific linear template was selected from the age-specific group at 33, 36 and 39PMW, respectively. The DTI-derived images and maps of this 33PMW, 36PMW or 39PMW single-subject were linearly normalized to the population-averaged-linear template in the 5th step to generate the single-subject template at 33, 36 and 39PMW, respectively. For tensor transformation, the affine transformation matrix and LDDMM transformation matrix obtained from the scalar images were applied to the tensor field to create normalized tensor fields (Xu et al., 2003). Such tensor transformations were conducted with *DiffeoMap* software (mrstudio.org).

2.4 Computation of Jacobian determinants

DTI datasets of 5 neonates at 33PMW, 5 neonates at 36PMW and 5 neonates at 39PMW (in total 15 neonates) were registered to the established age-specific single-subject templates at 33, 36 and 39PMW using a dual-channel LDDMM registration with FA and MD maps to drive the transformations. 9 transformation matrices were then generated. Logarithms of the Jacobian determinants of the entire brain were computed based on LDDMM transformation matrices with details in our previous publication (Huang et al., 2005). Averaged Jacobian determinants of the entire brain based on 9 transformation matrices were calculated. To demonstrate the morphological differences of five 33PMW subject brains from the 33PMW, 36PMW or 39PMW template, the maps of Jacobian determinant were generated based on transformation of five 33PMW brains to the single-subject templates at 33, 36 or 39PMW. Accordingly, the regional volumetric changes at frontal, parietal, temporal and occipital lobes were measured and the histograms of the regional volumetric changes were established with the whole brain Jacobian determinant maps obtained above.

2.5 Establishment of the age-specific DTI atlases at 33, 36 and 39PMW

The annotation and labeling of the major WM and GM structures were conducted on the single-subject templates at 33, 36 and 39PMW. Available atlases (Bayer and Altman, 2004;

Huang et al., 2009; Oishi et al., 2011) were adopted for neuroanatomical guidance. DTI-derived maps or images offer high contrasts for cerebral cortical gyri, subcortical nuclei and WM tracts. The contrasts in co-registered DTI OEC map, FA map, MD map, RD map, averaged DWI (aDWI) and b0 image were used for manual delineation of various neural structures. The labels from JHU neonate DTI atlas (Oishi et al., 2011) were first transformed to the SS template brain at 33, 36 and 39PMW with *DiffeoMap* software (mristudio.org) as initial labels of the age-specific atlases. These initial labels only provided rough contours. It is noteworthy that labels of “all” neural structures were manually adjusted and refined with neuroanatomists’ (L.F. and H.L.) months of manual work following the protocol below. Extensive manual delineation on the 2D axial, coronal or sagittal plane of the DTI-derived maps or images was conducted using ROIEditor (<http://www.mristudio.org>) to adjust the boundary of all neural structures. The manual delineation was mainly performed on the axial planes followed by manually adjusting the anatomical labels on the coronal and sagittal planes. Manual adjusting and refining processes conducted by the two neuroanatomists (L.F. and H.L.) were under the guidance of the major contributor (K.O.) of JHU neonate atlas. The annotations and labels of all major GM structures, including the cerebral cortex and subcortical nuclei, were conducted with contrasts of the MD maps and aDWI images. All major WM tracts were manually delineated on the DTI OEC maps. WM tracts that are adjacent to the subcortical nuclei, such as external capsule (ec) and anterior limb, posterior limb and retrolenticular part of internal capsule (alic, plic and rlic), were delineated with the contrasts of DTI OEC maps as well as FA maps and aDWI images. The ventricles were delineated with the contrasts of aDWI images.

To achieve accurate labeling, the cerebral cortex and subcortical nuclei were three-dimensionally (3D) reconstructed with Amira (FEI, Hillsboro, OR) so that cross-sectional boundaries of the 3D reconstructed parcellated cortical gyral surfaces and subcortical nuclei were used to refine the labeling. Similarly, the WM tracts were 3D reconstructed by DTI tractography (Mori et al., 1999) for accurately identifying location and boundary of these WM tracts. The processes of manual delineation on the 2D planes of certain view (e.g. axial) followed by adjustment on the 2D planes of other two (e.g. coronal and sagittal) views were repeated several times. In this way, the unsmooth boundary lines of 2D slices were improved until the boundaries of every labeled neural structure in all three views (axial, coronal and sagittal) became smooth. A total of 126 comprehensive GM and WM structures were delineated and annotated, as shown in the appendix. The above-mentioned procedures were also conducted to establish the comprehensive macaque brain atlas (Feng et al., 2017) and proved to be effective.

2.6 Evaluation of the age-specific atlases for automated labeling

To test using the age-specific atlases for automated labeling, 10 brain structures including 6 WM tracts, 2 subcortical nuclei and 2 cortical gyri were selected for quantitative evaluation. For testing, datasets of 5 subjects in each age group (in total 15 subjects) were randomly selected excluding the subjects used for establishing the single-subject templates. Dice’s coefficient and L1 error were used to evaluate reliability and misclassification error, respectively. 10 brain structures on the 2D images in native space were manually delineated by two raters (L.F. and L.S.) to investigate inter-rater variability. Notably the manual

delineation from these two raters was used to establish the atlases in the present study. The manual labeling results served as references for measuring labeling accuracy. Automated labels of the neural structures of 33, 36 and 39 PMW brains were obtained with reverse mapping of the transformation from the individual subject to population-averaged-nonlinear template.

For quantitative evaluation, the manual and automated delineation of 10 brain structures were saved as binary maps. The two binary maps from manual and automated delineate of every brain structure were overlaid. All voxels of the binary maps were then categorized into three groups: (1) voxels that were outside the structure in both delineations (nn); (2) voxels that were inside the structure in only one of these two delineations (pn, np); and (3) voxels that were inside the structure in both delineations (pp). The Dice ratio and L1 error were analyzed using the equations as following:

$$\text{Dice} = 2pp / (2pp + np + pn)$$

$$\text{L1} = (1 - pp / (pp + np + pn)) / 2$$

The Dice ratio and L1 error measurements within the manual trials by two different raters provided the level of precision for manual delineation, which was considered as the gold standard. Then, the Dice ratio and L1 error measurements comparing the automated and manual delineation were calculated for each structure.

2.7 Tract-wise microstructural measurement based on atlas WM labels

For illustrating possible application of these established age-specific DTI atlases, these atlases were mapped to the DTI data of 84 neonates included in the present study to reveal the microstructural development of WM tracts. Specifically, WM labels of a certain age-specific atlas was first mapped to the individual subject in the native space to obtain WM tract-wise regions-of-interests (ROIs). For each individual subject, the selection of 33PMW, 36PMW or 39PMW age-specific atlas was based on age category of this subject, shown in Figure 1. The mapping from atlas to the individual space is the reverse of transformation from the individual subject to population-averaged-nonlinear template obtained from *DiffeoMap* software (mristudio.org). DTI-derived metric (FA, MD, RD and AD) measurements of certain WM tracts were then obtained for 84 neonates using these tract-wise ROIs. The age-dependent FA, RD, MD and RD slope, representing microstructural developmental rate of each WM tract, was calculated. To reveal the distinctive microstructural development of categorized WM tracts, relationship of FA slopes versus MD slopes and relationship of RD slopes versus AD slopes for all tracts was demonstrated. All WM tracts were categorized into five functionally distinguished tract groups, namely commissural, association, limbic, projection and brainstem tract groups (e.g. Wakana, et al., 2004; Huang, et al., 2012). Linear fitting of FA, MD, AD and RD measurements of the following five tracts representing five tract groups was conducted to demonstrative heterogeneous microstructural development among WM tract groups: corpus callosum (cc: representing commissural tract group), superior corona radiata (scr: representing projection

tract group), fornix (fx: representing limbic tract group), inferior fronto-occipital fasciculus (ifo: representing association tract group), and inferior cerebellar peduncle (icp: representing brainstem tract group).

3. Results

3.1 Large morphological changes from 33PMW to 39PMW

The entire brain morphological changes among 33, 36 to 39PMW age groups are demonstrated with Jacobian determinant measurements shown in Figure 2. Smallest Jacobian determinants are shown at the diagonal entries with age of the test subject same as that of the template. Larger absolute Jacobian determinants were found with bigger age difference between age of the test subject and that of the template.

As shown in the Jacobian determinant maps in Figure 3, higher local volume expansions (Jacobian determinant greater than 1) are apparent in frontal and temporal areas from 33PMW to 36PMW (middle panels of Figure 3a) and from 33PMW to 39PMW (bottom panels of Figure 3a). Figure 3b shows the mean Jacobian determinants from normalizing 33PMW subject brains to the target template brain at 33PMW (green), 36PMW (blue) and 39PMW (red). The Jacobian determinants are significantly different ($p < 0.001$) with the target template at different ages (33PMW, 36PMW and 39PMW) for most of the brain lobes. The local volume increases are largest in the temporal lobe followed by frontal, occipital and parietal lobe, as shown in Figure 3b. Figure 3c shows the profile of local volume changes from 33PMW subject brain to the template brain at 33, 36 and 39PMW. The center of the Jacobian determinant histogram with the transformation from 33PMW subject brains to the 33PMW template brain is close to 1 while the center of the Jacobian determinant histogram with the transformation from 33PMW subject brains to the 39PMW template brain shifts to around 1.2.

3.2 Single-subject and population-averaged age-specific DTI templates at 33, 36 and 39PMW

Population-averaged-linear, population-averaged-nonlinear and SS b0 images, FA maps and DEC maps at 33, 36 and 39PMW are demonstrated in Figure 4. As pointed by the yellow arrows in the FA maps, high cortical FA shown as a bright band in the cortical plate are clear in the younger template brains at 33PMW and 36PMW. However, this bright cortical band is no longer visible in the template brain at 39PMW. Preservation of higher cortical FA in the population-averaged-nonlinear template at 33PMW and 36PMW also demonstrates quality of the nonlinear registration for generating the template. Besides clear microstructural changes, remarkable macrostructural changes such as cortical folding across 3 time points are apparent in the templates shown in Figure 4.

3.3 Age-specific DTI atlases at 33, 36 and 39 PMW

The comprehensive labels of 126 WM, cortical and subcortical neural structures on the SS template at 33PMW are shown in Figures 5–7. The labels are overlaid on high resolution axial, coronal and sagittal MD maps and OEC maps in Figure 5, 6 and 7, respectively. The locations of these 2D axial, coronal and sagittal planes are indicated by the orange lines on

the lower left corner of each figure. As shown in Figures 5–7, the boundaries of all parcellated neural structures look smooth and continuous in all three views. To demonstrate the neuroanatomical differences across the ages, the age-specific comprehensive labels of cortical gyri, subcortical nuclei and WM structures of 33, 36, and 39PMW are displayed side by side in one figure in the axial, coronal and sagittal planes in the Figure 8, Supplemental Figure 1 and Supplemental Figure 2, respectively. Each of these comprehensive age-specific neonate brain atlases at 33, 36 and 39PMW covers 52 cerebral cortical structures, 40 cerebral WM structures, 22 brainstem and cerebellar structures and 12 subcortical GM structures. The index table listing all labels of cortical gyri, WM structures and subcortical nuclei can be found in the Appendix. The enlarged regions in these figures show further details of the parcellated neural structures. The underlying image in left and right side of each panel in Figure 8 and supplemental Figure 1 is the OEC and MD map, respectively. In Supplemental Figure 2, the underlying image is the OEC maps in the first and third rows and MD maps in the second and fourth rows.

3.4 Dramatic neuroanatomical changes from 33PMW to 39PMW

With comprehensive labels of 33, 36 and 39PMW brains, anatomical changes of most neural structures from 33PMW to 39PMW can be well appreciated. Two representative examples of dramatic neuroanatomical changes are presented in Figure 9. The size decreases of GE from 33 to 36PMW until its final disappearance at around 39PMW are most striking. The structural changes of GE are highlighted by red arrows shown in Figure 9a. Figure 9b shows the significant size increases of uncinatus fasciculus (unc) highlighted by red arrows.

3.5 Evaluation of the age-specific atlases for automated labeling

The measurements of Dice ratio and L1 error in Figure 10 demonstrate the potential of these age-specific atlases for automated labeling of neonate brains at the age range of 31 to 42PMW. The Dice scores are over 0.8 in most regions between automated and manual delineation except in cingulate bundle in cingulate gyrus (cgc) and unc. As shown in Figure 10a, the Dice ratio of cgc and unc are also over 0.75. High Dice ratios (>0.8) indicate highly accurate automated labels. The relatively high Dice ratios (over 0.75) even in the thin and string-like structure of cgc indicate substantial accuracy of automated labeling. Misclassification of automated labeling measured by L1 errors (Figure 10b) is as low as that of manual labeling.

3.6 Microstructural development of WM tracts of preterm and term-born brains

With automated WM labels from the age-specific atlases as ROIs for tract-wise microstructural measurement, we found general age-related increases of FA and decreases of MD, AD and RD in all tested WM tracts. The scatter plots in Figure 11a and 11b show the relationship between the MD slopes and FA slopes and the relationship between the AD slopes and the RD slopes of all major WM tracts. Relatively more rapid age-related increases in FA and more rapid decreases in MD, AD and RD are shown in the projection tracts, with the biggest slopes of projection tracts scr, posterior corona radiata (pcr) and rlic clustered in the upper right corner of the Figure 11a and 11b. Meanwhile, relatively mild age-related increases in FA and mild decreases in MD, AD and RD are shown in the limbic tracts fx and cingulum bundle to hippocampus (cgh), clustered in the lower left corner of

Figure 11a and 11b. The age-related changes of five tracts, respectively representing five tract groups, are displayed in Figure 11c. Heterogeneous time-dependent changes of FA, MD, AD, and RD of these tracts are shown in Figure 11c, indicating heterogeneous microstructural maturation. Notably, with FA, MD, RD and AD measurements of the individual WM tracts, the microstructural change slopes of fornix (fx) representing limbic tract group are remarkably lower than those of corpus callosum (cc) and superior corona radiata (scr), representing commissural and projection tract group, respectively.

4. Discussion

The comprehensive age-specific brain DTI atlases at 33, 36 and 39PMW were established with each atlas covering 40 cerebral WM structures, 52 cerebral cortical structures, 22 brainstem and cerebellar structures and 12 deep GM structures. The age-specific population-averaged-linear, population-averaged-nonlinear and SS DTI templates were also generated. With dramatic morphological changes in the last 10 weeks before normal time of birth, age-specific atlases and templates are needed for accurate labeling of neural structures and mapping of the subject data to a common space. The quantitative evaluation with Dice ratio and L1 error was conducted by comparing the manual delineation to automated delineation from the established atlases. The evaluation results demonstrated high reproducibility and low misclassification errors of automated labels of both GM and WM structures. We also demonstrated that the age-specific atlases can be used to efficiently and effectively reveal the microstructural development of individual WM tracts by obtaining the tract-wise DTI-derived metric measurements automatically from the atlas labels. These established age-specific comprehensive GM and WM atlases and templates for 33, 36 and 39 PMW brains may be used for not only understanding the complicated yet precisely organized functional and structural maturational processes but also detecting neural disorder biomarkers of the preterm brains as clinical references. These atlases and templates are freely available through the website brainmrimap.org.

4.1 Age-specific digital DTI atlases and templates of 33, 36 and 39 PMW brains

From 31PMW to 42PMW, the brain morphology changes dramatically and heterogeneously (e.g. Kuklisova-Murgasova et al., 2011; Huang and Vasung, 2014; Ouyang et al., 2015; Yu et al., 2016). Overall brain size increases significantly in parallel with active cortical folding (e.g. Dubois, et al., 2008; Barkovich et al., 2012; Wright et al., 2014). Jacobian determinants have been used for quantitatively characterizing local volume changes during this developmental period (Figure 2 and 3). From Figure 2, the larger whole-brain absolute Jacobian determinants indicating larger overall deformation have been found between the brains with bigger age differences. Figure 3 demonstrated inhomogeneous local volume changes across the brain regions (Figure 3a) and lobes (Figure 3b). The results of the Jacobian determinant suggest it is critical to establish an age-specific atlas in this period with the neural structures across the brain growing rapidly and heterogeneously. The established age-specific templates could effectively alleviate biases in the process of registering subject brain images to the templates. Besides SS template, the established age-specific population-averaged DTI templates represent the brain images of a population of healthy preterm or term-born neonates and incorporate the individual variations of the subjects at certain ages.

They could be used as the templates for functional and structural research on early brain development.

Each of the established age-specific brain DTI atlases of 33, 36 and 39 PMW includes comprehensive neuroanatomical labels of 126 GM and WM structures (Figures 5–8 and Supplemental Figures 1–2). Based on relatively high isotropic DTI imaging resolution ($1.5 \times 1.5 \times 1.6 \text{ mm}^3$), these age-specific atlases offer the neuroanatomical labels in all axial, coronal and sagittal views, as also shown in Figures 5–8 and Supplemental Figures 1–2. Substantial manual delineation during the atlas creation process is critical for precise labels since most of the neural structures have irregular shapes but can be differentiated with high contrasts of DTI-derived maps. The manual delineation was mainly performed on the axial planes. Extensive adjustments in the coronal and sagittal planes were then made to achieve naturally smooth boundaries of all 126 labels in all three (axial, coronal and sagittal) planes. Many immature WM tracts cannot be differentiated with conventional relaxation-based MR images (T1- or T2-weighted) because of the insufficient myelination during the preterm development period. To our knowledge, little work has been done on delineation of individual WM tracts in the preterm population. Compared with the previous preterm and neonate templates or atlases (e.g. Altaye et al., 2008; Shi et al., 2011; Kuklisova-Murgasova et al., 2011; Makropoulos et al., 2014; Makropoulos et al., 2016) based on T1- or T2-weighted MRI, the present atlases are based on high resolution DTI data and can provide more comprehensive anatomic information of not only GM structures but also WM tracts. With these age-specific comprehensive DTI atlases at 33, 36 and 39PMW primarily focusing on preterm ages, they are complementary to the JHU-neonate atlas based on DTI of only term-born neonates (Oishi et al., 2011).

4.2 Dramatic changes of individual neural structures from 33 to 39PMW

Based on the delineation of individual neural structures (Figure 8, Supplemental Figure 1–2), relatively large morphological changes take place in most of the GM and WM structures among the 33, 36 and 39PMW brains. For example, the disappearance of GE, as observed from the age-specific atlas in Figure 9a, is most striking. GE is a transient developmental fetal brain structure. It has been clearly identified based on contrasts of DTI-derived maps of fetal brains (Huang et al., 2006; Huang et al., 2009). The size decreases of GE from 33 to 36 PMW with its final disappearance at around 39PMW can be clearly appreciated in Figure 9a. Additional label for GE at 33 and 36 PMW brain atlases is necessary for distinguishing GE from other subcortical nuclei. Besides GE, the size of certain WM tracts, such as unc, appears to increase significantly with age (Figure 9b). The disappearance of GE and dramatic size increases of unc in this period further demonstrated the importance of establishing age-specific brain atlases for preterm brains. The morphological information directly from the age-specific atlases, such as volume and shape, could be readily used for studying the development of other neural structures from 33PMW to 39PMW.

4.3 Evaluation of the automated labeling from the atlases

Delineation of ROIs based on neuroanatomy is critical for quantitative analysis of the functional, microstructural and physiological properties of various neural structures in the brain in health and disease. The presented atlases can be used for quantitative study on the

GM and WM development with the 3D ROIs generated by an automated method. This automated labeling from the atlases greatly enhances the efficiency of these quantitative studies especially when large sample size is included. To evaluate the reliability and misclassification errors, we compared manual delineation with automated labels from age-specific atlases by using the Dice ratio and L1 error to test how accurate the automated labels are. The Dice ratios of most of the structures were over 0.8 except *cgc* and *unc*, suggesting high level of accuracy of automated labeling (Figure 10a). With thin and string-like characteristics of *cgc* and *unc*, Dice ratios of these two structures were lower than those of other structures. Nevertheless, the Dice ratios of these two structures still over 0.75 indicate substantial registration accuracy for all tested brain structures. As shown in Figure 10, the high Dice ratios and low L1 errors from automated labeling suggest the atlas-based automated segmentation is reliable.

4.4 Application of the age-specific comprehensive atlases

To demonstrate using the age-specific DTI atlases, the FA, MD, AD and RD of the WM tracts in the 84 preterm and term-born brains were measured to reveal the microstructural development of these tracts. The FA, MD, AD and RD were measured with WM tract ROIs obtained by transferring the WM labels of these age-specific atlases to the subject brain. The developmental rates, i.e. the slopes of FA, MD, AD and RD measurements (Figures 11) from the atlas approach followed the typical maturational pattern described in the literature (e.g. Mukherjee et al., 2001; Gao et al., 2009; Oishi et al., 2011, 2013; Dubois et al., 2007, 2014; Akazawa et al., 2016) during the early developmental period. The water content in WM of the premature infant brain decreases gradually with the procedure of myelination (e.g. Deoni et al., 2011; Dubois et al., 2014). For most of the WM tracts, RD measurements decrease faster than AD measurements (Figure 11b), suggesting a more increased restriction in water diffusion perpendicular to the WM tract pathways than along them during this maturational period. Faster decreases of RD measurements than AD measurements result in increases in FA. From Figure 11, the age-related microstructural changes are significant for most of the WM tracts but heterogeneous among them. Relatively faster age-related increases in FA and faster decreases in MD, AD and RD were shown in the projection tract (*scr*) compared to the limbic tract (*fx*) (Figure 11c), suggesting faster maturation of the projection tracts from 31 to 42PMW. On the other hand, limbic tracts have been previously characterized with DTI as the WM tracts appearing earliest among all WM and mature rapidly before the 3rd trimester (Huang et al., 2009; Huang et al, 2014; Takahashi et al, 2011; Yu et al., 2014; Ouyang et al., 2015).

With the comprehensive labels of not only WM tracts, but also cortical regions, these age-specific DTI atlases can be also used for delineating cortical ROIs for structural measurements such as cortical thickness (e.g. Li et al., 2015), physiological measurements such as cerebral blood flow (e.g. De Vis et al., 2013; Ouyang et al., 2017), and transcriptome profiling (e.g. Huang et al., 2013). The connective maturation of the neonate brain has been recently studied with noninvasive neuroimaging methods to understand emergence of functional (e.g. Doria, et al., 2010; Gao et al., 2011; Cao et al., 2017) and structural (e.g. Yap et al., 2011; Huang et al., 2015; Batalle et al., 2017; Song et al., 2017) networks. The GM

labels of age-specific neonate brain atlases would be especially useful in the parcellation of the cerebral cortex into the nodes for investigating connectivity among brain regions.

4.5 Other considerations and future perspectives

This study is affected by several factors including preterm effects, imaging resolutions and sample size. Preterm birth has been widely recognized as one of the risk factors that might affect the normal brain development. The templates and atlases were generated with the DTI data of healthy preterm neonates without apparent neural abnormalities, as elaborated in the exclusion criteria in 2.1. Follow-up tests are ongoing to confirm typical development of the participating neonates. With small brain sizes of the neonates, the DTI imaging resolution of all neonates was $1.5 \times 1.5 \times 1.6 \text{ mm}^3$, higher than 2–3mm isotropic resolution usually used in adult brain DTI acquisition. The relatively high resolution facilitated better delineation of the neural structures. Despite the overall sample size of the recruited neonates being close to 100, the number of subjects in each age group is limited. With the advances of MR techniques, higher DTI spatial resolution and diffusion gradient angular resolution could be potentially used for establishing the age-specific atlases of the preterm and term-born neonate brains with more anatomical details. Using a larger sample size for each age group in the future could incorporate more extensive individual variances for the population-averaged templates. The accuracy of automated labeling from the established atlases to the subject brain is related to the quality of image registration. Dual-channel LDDMM registration could alleviate the registration bias caused by image intensity inconsistency in single-image contrast. Nevertheless, the accuracy of Jacobian determinants quantifying local volume differences in Figures 2 and 3 could still be affected by imperfection of image registration. Besides full tensor transformation method (Xu et al., 2003) used in the present study, other tensor transformation algorithms (e.g. Zhang et al., 2006; Yeo et al., 2009) could be evaluated for more accurate alignment of diffusion tensors when generating population-averaged templates in the future. All the presented age-specific DTI atlases and templates will be disseminated through the website www.brainmrimap.org. Establishing a software platform based on these atlases and templates for functional, structural and connective analyses could further promote the basic and clinical research on the developmental brains of preterm and term-born infants.

5 Conclusion

We established the age-specific DTI templates and atlases with comprehensive GM and WM labels for 33, 36 and 39PMW brains. These templates and atlases were generated with relatively high resolution DTI data of 84 healthy preterm and term-born neonates. The age-specific DTI templates consist of SS, population-averaged-linear and population-averaged-nonlinear template. Each of the age-specific DTI atlases includes 126 brain structures with smooth boundaries in all three (axial, coronal and sagittal) views. The automated labeling process by mapping the atlas labels to the subject data was found to be reliable and reproducible. These age-specific atlases and templates could be used for not only understanding the complicated yet precisely organized functional and structural maturational processes, but also detecting neural disorder biomarkers of the preterm brains as clinical

references. All established templates and atlases are disseminated through the website (<http://www.brainmrimap.org>).

Supplementary Material

Refer to Web version on PubMed Central for supplementary material.

Acknowledgments

This study was supported by the National Institutes of Health (NIH MH092535, NIH MH092535-04S1, NIH R01HD065955 and NIH 5RC2MH089921).

Appendix

Neuroanatomical labels of 126 gray and white matter structures and their abbreviations.

	Abbreviation	Structure	Left/right	33/36/39PMW
1	cc	corpus callosum	Left	33/36/39PMW
2	cc	corpus callosum	Right	33/36/39PMW
3	alic	anterior limb of internal capsule	Left	33/36/39PMW
4	alic	anterior limb of internal capsule	Right	33/36/39PMW
5	plic	posterior limb of internal capsule	Left	33/36/39PMW
6	plic	posterior limb of internal capsule	Right	33/36/39PMW
7	rlic	retrolenticular part of internal capsule	Left	33/36/39PMW
8	rlic	retrolenticular part of internal capsule	Right	33/36/39PMW
9	acr	anterior corona radiata	Left	33/36/39PMW
10	acr	anterior corona radiata	Right	33/36/39PMW
11	scr	superior corona radiata	Left	33/36/39PMW
12	scr	superior corona radiata	Right	33/36/39PMW
13	pcr	posterior corona radiata	Left	33/36/39PMW
14	pcr	posterior corona radiata	Right	33/36/39PMW
15	cgc	cingulum cingulate gyrus part	Left	33/36/39PMW
16	cgc	cingulum cingulate gyrus part	Right	33/36/39PMW
17	cgh	cingulum hippocampal part	Left	33/36/39PMW
18	cgh	cingulum hippocampal part	Right	33/36/39PMW
19	fx	fornix	Left	33/36/39PMW
20	fx	fornix	Right	33/36/39PMW
21	st	stria terminalis	Left	33/36/39PMW
22	st	stria terminalis	Right	33/36/39PMW
23	tap	tapetum	Left	33/36/39PMW
24	tap	tapetum	Right	33/36/39PMW
25	slf	superior longitudinal fasciculus	Left	33/36/39PMW
26	slf	superior longitudinal fasciculus	Right	33/36/39PMW
27	ec	external capsule	Left	33/36/39PMW
28	ec	external capsule	Right	33/36/39PMW
29	ptr	posterior thalamic radiata	Left	33/36/39PMW

	Abbreviation	Structure	Left/right	33/36/39PMW
30	ptr	posterior thalamic radiata	Right	33/36/39PMW
31	ss	sagittal stratum	Left	33/36/39PMW
32	ss	sagittal stratum	Right	33/36/39PMW
33	Tha	thalamus	Left	33/36/39PMW
34	Tha	thalamus	Right	33/36/39PMW
35	Put	putamen	Left	33/36/39PMW
36	Put	putamen	Right	33/36/39PMW
37	GP	globus pallidus	Left	33/36/39PMW
38	GP	globus pallidus	Right	33/36/39PMW
39	Caud	caudate	Left	33/36/39PMW
40	Caud	caudate	Right	33/36/39PMW
41	cp	cerebral peduncle	Left	33/36/39PMW
42	cp	cerebral peduncle	Right	33/36/39PMW
43	sfo	superior fronto-occipital fasciculus	Left	33/36/39PMW
44	sfo	superior fronto-occipital fasciculus	Right	33/36/39PMW
45	ifo	inferior fronto-occipital fasciculus	Left	33/36/39PMW
46	ifo	inferior fronto-occipital fasciculus	Right	33/36/39PMW
47	cst	corticospinal tract	Left	33/36/39PMW
48	cst	corticospinal tract	Right	33/36/39PMW
49	scp	superior cerebellar peduncle	Left	33/36/39PMW
50	scp	superior cerebellar peduncle	Right	33/36/39PMW
51	mcp	middle cerebellar peduncle	Left	33/36/39PMW
52	mcp	middle cerebellar peduncle	Right	33/36/39PMW
53	icp	inferior cerebellar peduncle	Left	33/36/39PMW
54	icp	inferior cerebellar peduncle	Right	33/36/39PMW
55	pct	pontine crossing tract	Left	33/36/39PMW
56	pct	pontine crossing tract	Right	33/36/39PMW
57	unc	uncinate fasciculus	Left	33/36/39PMW
58	unc	uncinate fasciculus	Right	33/36/39PMW
59	midbrain	midbrain	Left	33/36/39PMW
60	midbrain	midbrain	Right	33/36/39PMW
61	pons	pons	Left	33/36/39PMW
62	pons	pons	Right	33/36/39PMW
63	ml	medial lemniscus	Left	33/36/39PMW
64	ml	medial lemniscus	Right	33/36/39PMW
65	medulla	medulla oblongata	Left	33/36/39PMW
66	medulla	medulla oblongata	Right	33/36/39PMW
67	SFG	superior frontal gyrus	Left	33/36/39PMW
68	SFG	superior frontal gyrus	Right	33/36/39PMW
69	MFG	middle frontal gyrus	Left	33/36/39PMW
70	MFG	middle frontal gyrus	Right	33/36/39PMW
71	IFG	inferior frontal gyrus	Left	33/36/39PMW

	Abbreviation	Structure	Left/right	33/36/39PMW
72	IFG	inferior frontal gyrus	Right	33/36/39PMW
73	MFOG	medial fronto-orbital gyrus	Left	33/36/39PMW
74	MFOG	medial fronto-orbital gyrus	Right	33/36/39PMW
75	LFOG	lateral fronto-orbital gyrus	Left	33/36/39PMW
76	LFOG	lateral fronto-orbital gyrus	Right	33/36/39PMW
77	RG	gyrus rectus	Left	33/36/39PMW
78	RG	gyrus rectus	Right	33/36/39PMW
79	PrCG	precentral gyrus	Left	33/36/39PMW
80	PrCG	precentral gyrus	Right	33/36/39PMW
81	PoCG	postcentral gyrus	Left	33/36/39PMW
82	PoCG	postcentral gyrus	Right	33/36/39PMW
83	SPL	superior parietal gyrus	Left	33/36/39PMW
84	SPL	superior parietal gyrus	Right	33/36/39PMW
85	PrCu	precuneus	Left	33/36/39PMW
86	PrCu	precuneus	Right	33/36/39PMW
87	CingG	cingulate gyrus	Left	33/36/39PMW
88	CingG	cingulate gyrus	Right	33/36/39PMW
89	SMG	supramarginal gyrus	Left	33/36/39PMW
90	SMG	supramarginal gyrus	Right	33/36/39PMW
91	AG	angular gyrus	Left	33/36/39PMW
92	AG	angular gyrus	Right	33/36/39PMW
93	STG	superior temporal gyrus	Left	33/36/39PMW
94	STG	superior temporal gyrus	Right	33/36/39PMW
95	MTG	middle temporal gyrus	Left	33/36/39PMW
96	MTG	middle temporal gyrus	Right	33/36/39PMW
97	ITG	inferior temporal gyrus	Left	33/36/39PMW
98	ITG	inferior temporal gyrus	Right	33/36/39PMW
99	FuG	fusiform gyrus	Left	33/36/39PMW
100	FuG	fusiform gyrus	Right	33/36/39PMW
101	PHG	parahippocampal gyrus	Left	33/36/39PMW
102	PHG	parahippocampal gyrus	Right	33/36/39PMW
103	ENT	entorhinal gyrus	Left	33/36/39PMW
104	ENT	entorhinal gyrus	Right	33/36/39PMW
105	SOG	superior occipital gyrus	Left	33/36/39PMW
106	SOG	superior occipital gyrus	Right	33/36/39PMW
107	MOG	middle occipital gyrus	Left	33/36/39PMW
108	MOG	middle occipital gyrus	Right	33/36/39PMW
109	IOG	inferior occipital gyrus	Left	33/36/39PMW
110	IOG	inferior occipital gyrus	Right	33/36/39PMW
111	Cu	cuneus	Left	33/36/39PMW
112	Cu	cuneus	Right	33/36/39PMW
113	LG	lingual gyrus	Left	33/36/39PMW

	Abbreviation	Structure	Left/right	33/36/39PMW
114	LG	lingual gyrus	Right	33/36/39PMW
115	Amyg	amygdala	Left	33/36/39PMW
116	Amyg	amygdala	Right	33/36/39PMW
117	Hippo	hippocampus	Left	33/36/39PMW
118	Hippo	hippocampus	Right	33/36/39PMW
119	Cerebellum	cerebellar hemisphere	Left	33/36/39PMW
120	Cerebellum	cerebellar hemisphere	Right	33/36/39PMW
121	Ins	insular cortex	Left	33/36/39PMW
122	Ins	insular cortex	Right	33/36/39PMW
123	ac	anterior commissure	Left	33/36/39PMW
124	ac	anterior commissure	Right	33/36/39PMW
125	GE	ganglionic eminence	Left	33/36PMW
126	GE	ganglionic eminence	Right	33/36PMW

References

- Akazawa K, Chang L, Yamakawa R, Hayama S, Buchthal S, Alicata D, Andres T, Castillo D, Oishi K, Skranes J, Ernst T, Oishi K, 2016 Probabilistic maps of the white matter tracts with known associated functions on the neonatal brain atlas: application to evaluate longitudinal developmental trajectories in term-born and preterm-born infants. *Neuroimage* 128, 167–179. [PubMed: 26712341]
- Altaye M, Holland SK, Wilke M, Gaser C, 2008 Infant brain probability templates for MRI segmentation and normalization. *Neuroimage* 43, 721–730. [PubMed: 18761410]
- Ball G, Aljabar P, Zebari S, Tumor N, Arichi T, Merchant N, Robinson EC, Ogundipe E, Rueckert D, Edwards AD, et al. 2014 Rich-club organization of the newborn human brain. *Proc Natl Acad Sci USA*. 111:7456–7461. [PubMed: 24799693]
- Barkovich AJ, Guerrini R, Kuzniecky RI, Jackson GD, Dobyns WB, 2012 A developmental and genetic classification for malformations of cortical development: update 2012. *Brain* 135, 1348–1369. [PubMed: 22427329]
- Batalle D, Hughes EJ, Zhang H, Tournier JD, Tumor N, Aljabar P, Wali L, Alexander DC, Hajnal JV, Nosarti C, Edwards AD, Counsell SJ, 2017 Early development of structural networks and the impact of prematurity on brain connectivity. *Neuroimage* 149, 379–392. [PubMed: 28153637]
- Bayer SA, Altman J, 2004 ‘The human brain during the third trimester’. CRC Press.
- Beaulieu C, 2002 The basis of anisotropic water diffusion in the nervous system—a technical review. *NMR Biomed* 15, 435–455. [PubMed: 12489094]
- Bystron I, Blakemore C, Rakic P, 2008 Development of the human cerebral cortex: boulder committee revisited. *Nat. Rev. Neurosci* 9, 110–122. [PubMed: 18209730]
- Cao M, He Y, Dai Z, Liao X, Jeon T, Ouyang M, Chalak L, Bi Y, Rollins N, Dong Q, Huang H, 2017 Early development of functional network segregation revealed by connectomic analysis of the preterm human brain. *Cereb. Cortex* 27, 1949–1963. [PubMed: 26941380]
- Ceritoglu C, Oishi K, Li X, Chou MC, Younes L, Albert M, Lyketsos C, van Zijl PC, Miller MI, Mori S, 2009 Multi-contrast large deformation diffeomorphic metric mapping for diffusion tensor imaging. *Neuroimage* 47, 618–627. [PubMed: 19398016]
- De Vis JB, Petersen ET, de Vries LS, Groenendaal F, Kersbergen KJ, Alderliesten T, Hendrikse J, Benders MJ, 2013 Regional changes in brain perfusion during brain maturation measured non-invasively with Arterial Spin Labeling MRI in neonates. *Eur J Radiol*. 82, 538–543. [PubMed: 23199750]

- Deoni SC, Mercure E, Blasi A, Gasston D, Thomson A, Johnson M, Murphy DG, 2011 Mapping infant brain myelination with magnetic resonance imaging. *J. Neurosci* 31, 784–791. [PubMed: 21228187]
- Doria V, Beckmann CF, Arichi T, Merchant N, Groppo M, Turkheimer FE, Counsell SJ, Murgasova M, Aljabar P, Nunes RG, et al. 2010 Emergence of resting state networks in the preterm human brain. *Proc Natl Acad Sci USA*. 107:20015–20020. [PubMed: 21041625]
- Dubois J, Hertz-Pannier L, Dehaene-Lambertz G, Cointepas Y, Le Bihan D, 2006 Assessment of the early organization and maturation of infants' cerebral white matter fiber bundles: a feasibility study using quantitative diffusion tensor imaging and tractography. *Neuroimage* 30, 1121–1132. [PubMed: 16413790]
- Dubois J, Benders M, Borradori-Tolsa C, Cachia A, Lazeyras F, Ha-Vinh Leuchter R, Sizonenko SV, Warfield SK, Mangin JF, Huppi PS, 2008 Primary cortical folding in the human newborn: an early marker of later functional development. *Brain* 131, 2028–2041. [PubMed: 18587151]
- Dubois J, Dehaene-Lambertz G, Kulikova S, Poupon C, Huppi PS, Hertz-Pannier L, 2014 The early development of brain white matter: a review of imaging studies in fetuses, newborns and infants. *Neuroscience* 276, 48–71. [PubMed: 24378955]
- Dubois J, Dehaene-Lambertz G, Perrin M, Mangin JF, Cointepas Y, Duchesnay E, Le Bihan D, Hertz-Pannier L, 2008 Asynchrony of the early maturation of white matter bundles in healthy infants: quantitative landmarks revealed noninvasively by diffusion tensor imaging. *Hum. Brain Mapp* 29, 14–27. [PubMed: 17318834]
- Engle WA, American Academy of Pediatrics Committee on Fetus and Newborn, 2004 Age terminology during the perinatal period. *Pediatrics* 114, 1362–1364. [PubMed: 15520122]
- Feng L, Jeon T, Yu. Q, Ouyang M, Peng. Q, Mishra. V, Pletikos. M, Sestan. N, Miller. MI, Mori. S, Hsiao. S, Liu. S, Huang H, 2017 Population-averaged atlas with high-resolution ex vivo DTI integrated into in vivo space. *Brain Struct Funct* 222: 4131–4147. [PubMed: 28634624]
- Gao W, Lin W, Chen Y, Gerig G, Smith JK, Jewells V, Gilmore JH, 2009 Temporal and spatial development of axonal maturation and myelination of white matter in the developing brain. *AJNR Am. J. Neuroradiol* 30, 290–296. [PubMed: 19001533]
- Gao W, Gilmore JH, Giovanello KS, Smith JK, Shen D, Zhu H, Lin W, 2011 Temporal and spatial evolution of brain network topology during the first two years of life. *PLoS One*. 6: e25278. [PubMed: 21966479]
- Geng X, Gouttard S, Sharma A, Gu H, Styner M, Lin W, Gerig G, Gilmore JH, 2012 Quantitative tract-based white matter development from birth to age 2 years. *Neuroimage* 61, 542–557. [PubMed: 22510254]
- Huang H, Zhang J, Jiang H, Wakana S, Poetscher L, Miller MI, van Zijl PCM, Hillis AE, Wytik R, Mori S, 2005 DTI Tractography based Parcellation of White Matter: Application to the Mid-sagittal Morphology of Corpus Callosum. *NeuroImage* 26: 195–205. [PubMed: 15862219]
- Huang H, Zhang J, Wakana S, Zhang W, Ren T, Richards LJ, Yarowsky P, Donohue P, Graham E, van Zijl PC, Mori S, 2006 White and gray matter development in human fetal, newborn and pediatric brains. *Neuroimage* 33, 27–38. [PubMed: 16905335]
- Huang H, Xue R, Zhang J, Ren T, Richards LJ, Yarowsky P, Miller MI, Mori S, 2009 Anatomical characterization of human fetal brain development with diffusion tensor magnetic resonance imaging. *J. Neurosci* 29, 4263–4273. [PubMed: 19339620]
- Huang H, 2010 Structure of the fetal brain: what we are learning from DTI. *Neuroscientist* 16, 634–649. [PubMed: 20360600]
- Huang H, Vasung L, 2014 Gaining insight of fetal brain development with diffusion MRI and histology. *Int. J. Dev. Neurosci*, 32, 11–22. [PubMed: 23796901]
- Huang H, Fan X, Weiner M, Martin-Cook K, Xiao G, Davis J, Devous M, Rosenberg R, Diaz-Arrastia R, 2012 Distinctive disruption patterns of white matter tracts in Alzheimer's disease with full diffusion tensor characterization. *Neurobiol. Aging* 33, 2029–2045 [PubMed: 21872362]
- Huang H, Jeon T, Sedmak G, Pletikos M, Vasung L, Xu X, Yarowsky P, Richards L, Kostovic I, Sestan N, Mori S, 2013 Coupling diffusion imaging with histological and gene expression analysis to examine the dynamics of cortical areas across the fetal period of human brain development. *Cereb. Cortex* 23, 2620–2631. [PubMed: 22933464]

- Huang H, Shu N, Mishra V, Jeon T, Chalak L, Wang ZJ, Rollins N, Gong G, Cheng H, Peng Y, Dong Q, He Y, 2015 Development of human brain structural networks through infancy and childhood. *Cereb. Cortex* 25, 1389–1404. [PubMed: 24335033]
- Huang H, Vasung L, 2014 Gaining insight of fetal brain development with diffusion MRI and histology. *Int. J. Dev. Neurosci* 32, 11–22. [PubMed: 23796901]
- Huppi PS, Inder TE, 2001 Magnetic resonance techniques in the evaluation of the perinatal brain: recent advances and future directions. *Semin Neonatol* 6,195–210. [PubMed: 11483024]
- Huppi PS, Maier SE, Peled S, Zientara GP, Barnes PD, Jolesz FA, Volpe JJ, 1998 Microstructural development of human newborn cerebral white matter assessed *in vivo* by diffusion tensor magnetic resonance imaging. *Pediatr. Res* 44, 584–590. [PubMed: 9773850]
- Huppi PS, Murphy B, Maier SE, Zientara GP, Inder TE, Barnes PD, Kikinis R, Jolesz FA, Volpe JJ, 2001 Microstructural brain development after perinatal cerebral white matter injury assessed by diffusion tensor magnetic resonance imaging. *Pediatrics* 107:455–60. [PubMed: 11230582]
- Kazemi K, Ghadimi S, Abrishami-Moghaddam H, Grebe R, Gondry-Jouet C, Wallois F, 2008 Neonatal probabilistic models for brain, CSF and skull using T1-MRI data: preliminary results. *Conf. Proc. IEEE Eng. Med. Biol. Soc* 3892–3895. [PubMed: 19163563]
- Kostovic I, Jovanov-Milosevic N, 2006 The development of cerebral connections during the first 20–45 weeks' gestation. *Semin. Fetal Neonatal Med* 11,415–422. [PubMed: 16962836]
- Kuklisova-Murgasova M, Aljabar P, Srinivasan L, Counsell SJ, Doria V, Serag A, Gousias IS, Boardman JP, Rutherford MA, Edwards AD, Hajnal JV, Rueckert D, 2011 A dynamic 4D probabilistic atlas of the developing brain. *Neuroimage* 54, 2750–2763. [PubMed: 20969966]
- Li G, Wang L, Shi F, Gilmore JH, Li W, Shen D, 2015 Construction of 4D high-definition cortical surface atlases of infants: Methods and applications. *Med Image Anal* 25, 22–36. [PubMed: 25980388]
- Ling X, Tang W, Liu G, Huang L, Li B, Li X, Liu S, Xu J, 2013 Assessment of brain maturation in the preterm infants using diffusion tensor imaging (DTI) and enhanced T2 star weighted angiography (ESWAN). *Eur. J. Radiol* 82, 476–483.
- Makropoulos A, Gousias IS, Ledig C, Aljabar P, Hajnal JV, Edwards AD, Counsell SJ, Rueckert D, 2014 Automatic whole brain MRI segmentation of developing neonate brain. *IEEE Trans Med Imaging* 33, 1818–1831. [PubMed: 24816548]
- Makropoulos A, Aljabar P, Wright R, Huning B, Merchant N, Arichi T, Tumor N, Hajnal JV, Edwards AD, Counsell SJ, Rueckert D, 2016 Regional growth and atlas of the developing human brain. *Neuroimage* 125, 456–478. [PubMed: 26499811]
- Miller MI, Trounev A, Younes L, 2002 On the metrics and euler-lagrange equations of computational anatomy. *Ann. Rev. Biomed. Eng* 4, 375–405. [PubMed: 12117763]
- Moeskops P, Benders MJ, Chit SM, Kersbergen KJ, Groenendaal F, De Vries LS, Viergever MA, Isgum I, 2015 Automatic segmentation of MR brain images of preterm infants using supervised classification. *Neuroimage* 118, 628–641. [PubMed: 26057591]
- Mori S, Crain BJ, Chacko VP, and van Zijl PC, 1999 Three-dimensional tracking of axonal projections in the brain by magnetic resonance imaging. *Ann. Neurol* 45, 265–269. [PubMed: 9989633]
- Mori S, Oishi K, Jiang H, Jiang L, Li X, Akhter K, Hua K, Faria AV, Mah-mood A, Woods R, Toga AW, Pike GB, Neto PR, Evans A, Zhang J, Huang H, Miller MI, Van ZP, Mazziotta J, 2008 Stereotaxic white matter atlas based on diffusion tensor imaging in an ICBM template. *Neuroimage* 40, 570–582. [PubMed: 18255316]
- Mukherjee P, Miller JH, Shimony JS, Conturo TE, Lee BC, Almlri CR, McKinstry RC, 2001 Normal brain maturation during childhood: developmental trends characterized with diffusion-tensor MR Imaging. *Radiology* 221, 349–358. [PubMed: 11687675]
- Neil JJ, Miller J, Mukherjee P, Huppi PS, 2002 Diffusion tensor imaging of normal and injured developing human brain - a technical review. *NMR Biomed* 15:543–552. [PubMed: 12489100]
- Oishi K, Zilles K, Amunts K, Faria A, Jiang H, Li X, Akhter K, Hua K, Woods R, Toga AW, Pike GB, Rosa-Neto P, Evans A, Zhang J, Huang H, Miller MI, van Zijl PC, Mazziotta J, Mori S, 2008 Human Brain White Matter Atlas: Identification and Assignment of Common Anatomical Structures in Superficial White Matter. *Neuroimage* 43, 447–457. [PubMed: 18692144]

- Oishi K, Mori S, Donohue PK, Ernst T, Anderson L, Buchthal S, Faria A, Jiang H, Li X, Miller MI, Van Zijl PCM, Chang L, 2011 Multi-contrast human neonatal brain atlas: application to normal neonate developmental analysis. *Neuroimage* 56, 8–20. [PubMed: 21276861]
- Oishi K, Faria AV, Yoshida S, Chang L, Mori S, 2013 Quantitative evaluation of brain development using anatomical MRI and diffusion tensor imaging. *Int. J. Dev. Neurosci* 31, 512–524. [PubMed: 23796902]
- Ouyang A, Jeon T, Sunkin SM, Pletikos M, Sedmak G, Sestan N, Lein ES, Huang H, 2015 Mapping of structural and connectional imaging data for the developing human brain with diffusion tensor imaging. *Methods* 73, 27–37. [PubMed: 25448302]
- Ouyang M, Liu P, Jeon T, Chalak L, Heyne R, Rollins NK, Licht DJ, Detre JA, Roberts TP, Lu H, Huang H, 2017a. Heterogeneous increases of regional cerebral blood flow during preterm brain development: Preliminary assessment with pseudo-continuous arterial spin labeled perfusion MRI. *NeuroImage*, 147, 233–242. [PubMed: 27988320]
- Prastawa M, Gilmore JH, Lin W, Gerig G, 2005 Automatic segmentation of MR images of the developing newborn brain. *Med. Image Anal* 9, 457–466. [PubMed: 16019252]
- Rose J, Vassar R, Cahill-Rowley K, Guzman XS, Stevenson DK, Barnea-Goraly N, 2014 Brain microstructural development at near-term age in very-low-birth-weight preterm infants: an atlas-based diffusion imaging study. *Neuroimage* 86, 244–256. [PubMed: 24091089]
- Rutherford M, Counsell S, Allsop J, Boardman J, Kapellou O, Larkman D, Hajnal J, Edwards D, Cowan F, 2004 *Pediatrics* 114: 1004–1014. [PubMed: 15466098]
- Rutherford M, Srinivasan L, Dyet L, Ward P, Allsop J, Counsell S, Cowan F, 2006 Magnetic resonance imaging in perinatal brain injury: clinical presentation, lesions and outcome. *Pediatr. Radiol* 36, 582–592. [PubMed: 16770663]
- Shi F, Yap PT, Wu G, Jia H, Gilmore JH, Lin W, Shen D, 2011 Infant brain atlases from neonates to 1- and 2-year-olds. *PLoS One*. 6, e18746. [PubMed: 21533194]
- Sidman RL, Rakic P, 1973 Neuronal migration, with special reference to developing human brain: a review. *Brain Res* 62, 1–35. [PubMed: 4203033]
- Song L, Mishra V, Ouyang M, Peng Q, Slinger M, Liu S, Huang H, 2017 Human fetal brain connectome: structural network development from middle fetal stage to birth. *Front. Neurosci* 11, 561. [PubMed: 29081731]
- Takahashi E, Folkert RD, Galaburda AM, Grant PE, 2011 Emerging cerebral connectivity in the human fetal brain: an MR tractography study. *Cereb. Cortex* 22, 455–464. [PubMed: 21670100]
- Thiebaut de Schotten M, Ffytche DH, Bizzi A, Dell'Acqua F, Allin M, Walshe M, Murray R, Williams SC, Murphy DG, Catani M, 2011 Atlasing location, asymmetry and inter-subject variability of white matter tracts in the human brain with MR diffusion tractography. *Neuroimage* 54, 49–59. [PubMed: 20682348]
- Toga AW, Thompson PM, Mori S, Amunts K, Zilles K, 2006 Towards multimodal atlases of the human brain. *Nat. Rev. Neurosci* 7, 952–966. [PubMed: 17115077]
- Vasung L, Huang H, Jovanov-Milosevic N, Pletikos M, Mori S, Kostovic I, 2010 Development of axonal pathways in the human fetal fronto-limbic brain: histochemical characterization and diffusion tensor imaging. *J Anat* 217, 400–417. [PubMed: 20609031]
- Weisenfeld NI, Warfield SK, 2009 Automatic segmentation of newborn brain MRI. *Neuroimage* 47, 564–572. [PubMed: 19409502]
- Wilson-Costello D, Friedman H, Minich N, Fanaroff AA, Hack M, 2005 Improved survival rates with increased neurodevelopmental disability for extremely low birth weight infants in the 1990s. *Pediatrics* 115, 997–1003. [PubMed: 15805376]
- Woodward LJ, Anderson PJ, Austin NC, Howard K, Inder TE, 2006 Neonatal MRI to predict neurodevelopmental outcomes in preterm infants. *New Engl J Med* 355: 685–694. [PubMed: 16914704]
- Wright R, Kyriakopoulou V, Ledig C, Rutherford MA, Hajnal JV, Rueckert D, Aljabar P, 2014 Automatic quantification of normal cortical folding patterns from fetal brain MRI. *Neuroimage* 91, 21–32. [PubMed: 24473102]
- Xu D, Mori S, Shen D, van Zijl PC, Davatzikos C, 2003 Spatial normalization of diffusion tensor fields. *Magn. Reson. Med* 50, 175–182. [PubMed: 12815692]

- Yap PT, Fan Y, Chen Y, Gilmore JH, Lin W, Shen D, 2011 Development trends of white matter connectivity in the first years of life. *PLoS ONE*. 6:e24678. [PubMed: 21966364]
- Yeo BTT, Vercauteren T, Fillard P, Peyrat JM, Pennec X, Golland P, Ayache N, Clatz O, 2009 DT-REFinD: Diffusion tensor registration with exact finite-strain differential. *IEEE Trans Med Imaging* 28, 1914–1928. [PubMed: 19556193]
- Yu Q, Ouyang A, Chalak L, Jeon T, Chia J, Mishra V, Sivarajan M, Jackson G, Rollins N, Liu S, Huang H, 2015 Structural development of human fetal and preterm brain cortical plate based on population-averaged templates. *Cereb. Cortex* 26, 4381–4391.
- Yu Q, Peng Y, Mishra V, Ouyang A, Li H, Zhang H, Chen M, Liu S, Huang H, 2014 Microstructure, length, and connection of limbic tracts in normal human brain development. *Front. Aging Neurosci* 6, 228. [PubMed: 25221509]
- Zhang H, Yushkevich PA, Alexander DC, Gee JC, 2006 Deformable registration of diffusion tensor MR images with explicit orientation optimization. *Med. Image Anal* 10, 764–785. [PubMed: 16899392]

Highlights

Dramatic structural changes during 3rd trimester require setup of age-specific atlas. Age-specific DTI templates were established with 84 preterm and term-born datasets. Age-specific DTI atlases at 33, 36 and 39 postmenstrual weeks were established. Each age-specific DTI atlas includes 126 comprehensive gray and white matter labels. The atlases can be used to measure the tract-based microstructures automatically.

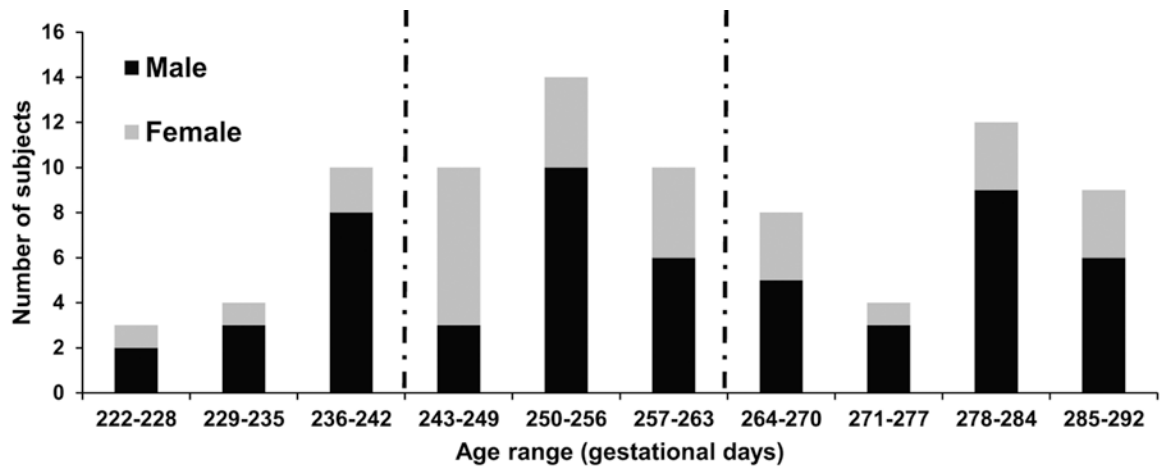


Figure 1:

The categorization of the 84 preterm and term-born neonate subjects used for establishing three age-specific atlases at 33, 36 and 39 PMW according to their ages at scan time. 17 preterm neonates scanned at 31.86 to 34.57 PMW, 34 preterm neonates scanned at 34.57 to 37.57 PMW and 33 preterm or term-born neonates scanned at 37.57 to 41.71 PMW were categorized into 33PMW, 36PMW and 39PMW group, respectively.

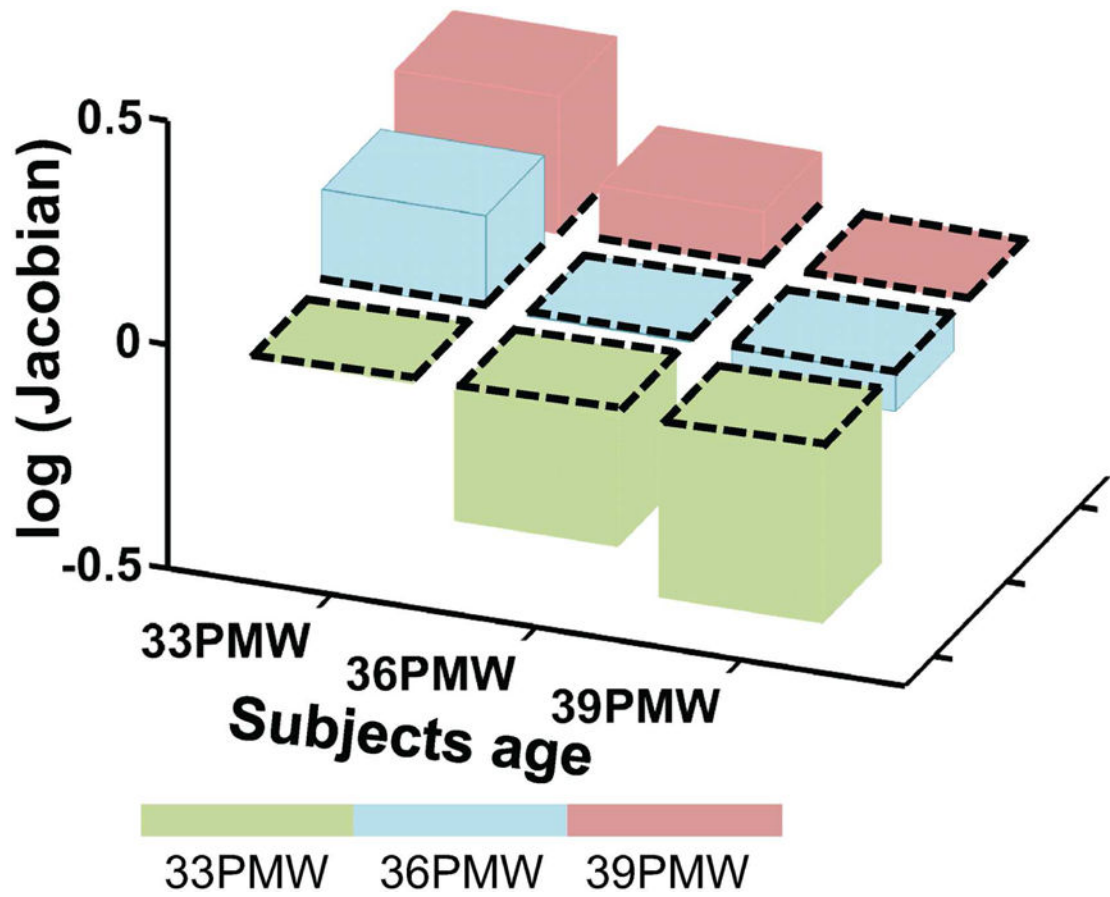


Figure 2: Whole brain Jacobian determinants of transformations of DTI data of 15 test subjects to single-subject template at 33, 36 and 39 PMW using nonlinear registration. Smallest Jacobian determinants at the diagonal entries were found with age of the test data subject same as that of the single-subject template. Larger absolute Jacobian determinants were found with bigger age difference between age of the test data subject and that of the single-subject template. The green, blue and red color indicates transformations to the single-subject template at 33, 36 and 39 PMW, respectively. The horizontal dashed lines in the 3D bar plot represent the zero plane.

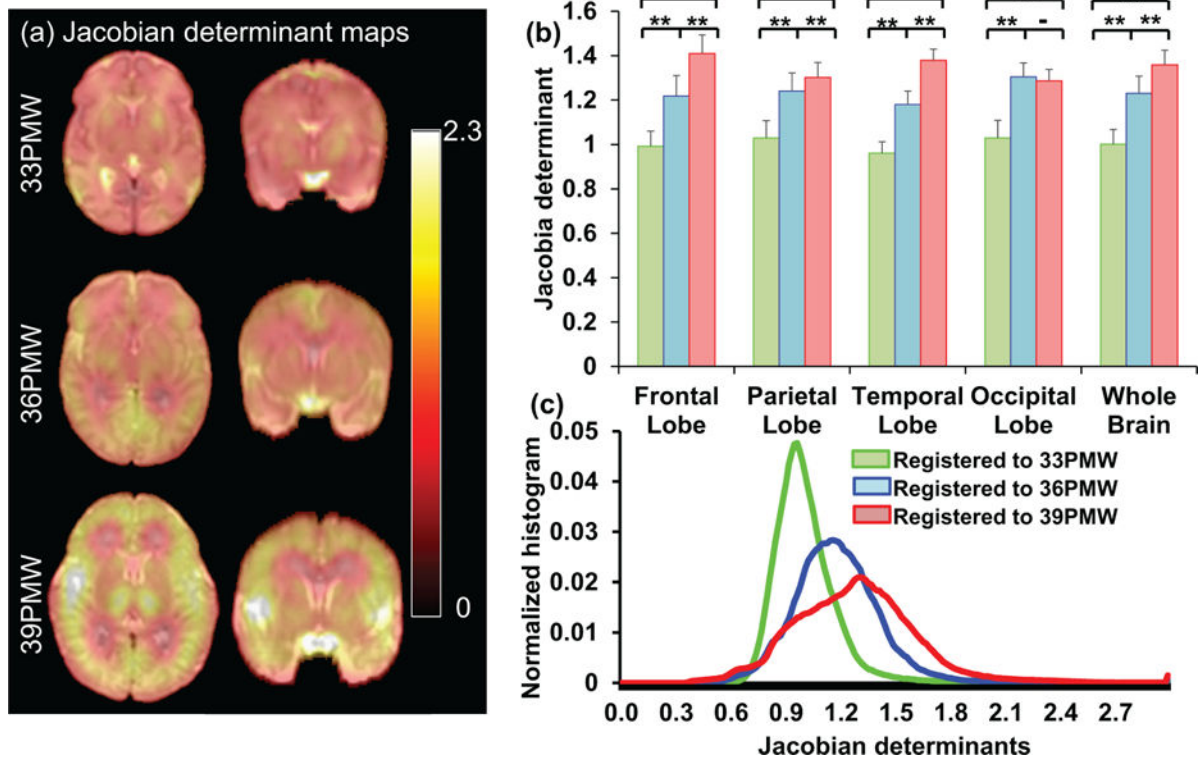


Figure 3:

Jacobian determinant maps overlaid on 33PMW (top panels), 36PMW (middle panels) and 39PMW b0 template (bottom panels) in (a) are based on registration of the five 33PMW subject brains to the single subject 33PMW, 36PMW and 39PMW template using nonlinear registration. Averages and standard errors of the Jacobian determinants at frontal, parietal, temporal, occipital lobes and whole brain with transformations from the five 33PMW subject brains to the single-subject 33PMW (green), 36PMW (blue) and 39PMW template (red) are shown in (b). Jacobian determinants are significantly different ($p < 0.01$) given the two templates at different ages (b). Normalized Jacobian determinant histogram showing distribution of the Jacobian determinant values with transformations from the five 33PMW subject brains to the 33PMW (green), 36PMW (blue) and 39PMW template (red) is shown in (c). Colorbar encodes Jacobian determinant values in (a). ** denotes $p < 0.001$ in (b).

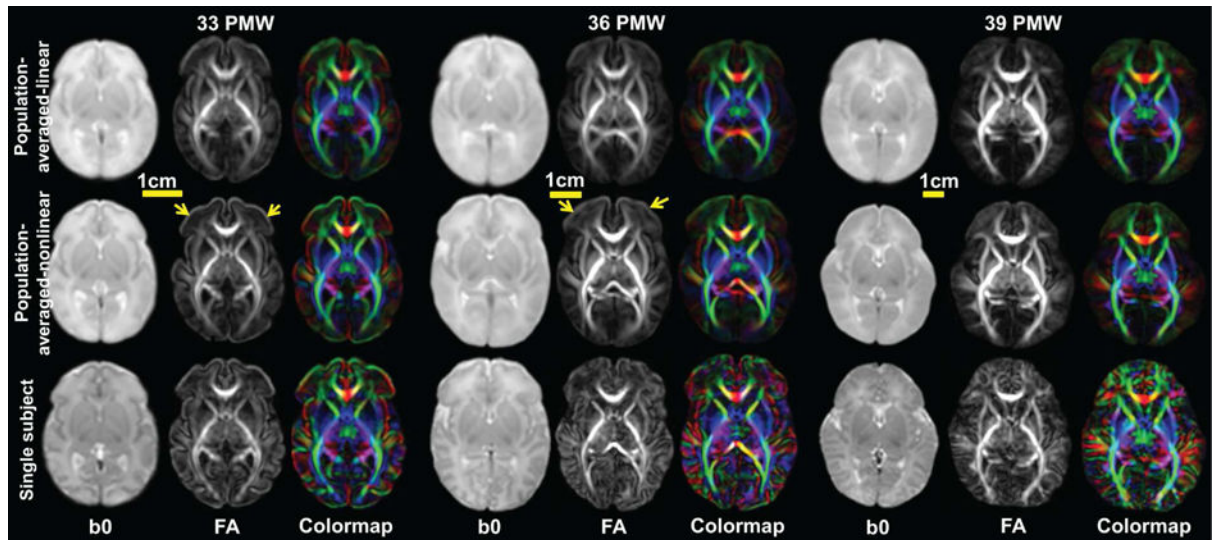


Figure 4: Population-averaged-linear (top panels), population-averaged-nonlinear (middle panels) and single-subject (lower panels) b0 images, FA maps and DTI colormaps (OEC maps) at 33PMW, 36PMW and 39PMW from left to right. Yellow arrows point to high cortical FA regions in the population-averaged-nonlinear template at 33 and 36PMW.

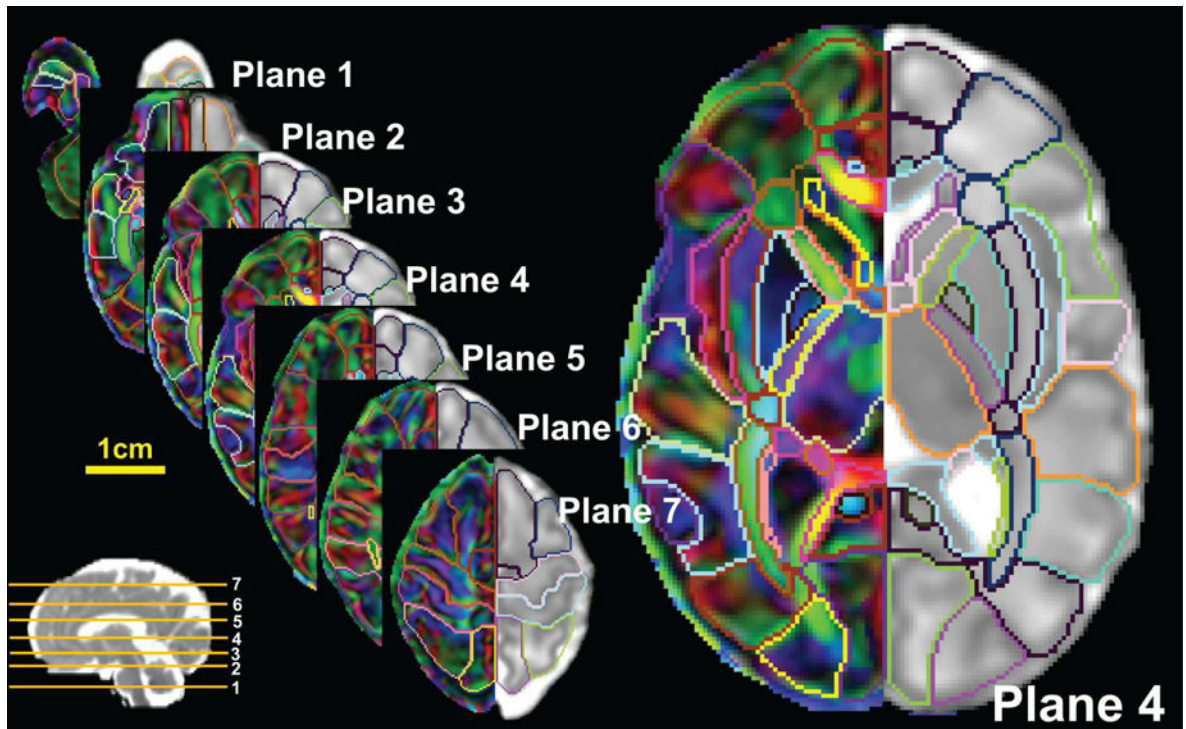


Figure 5:

Axial planes of the established preterm brain atlas at 33PMW with comprehensive GM and WM labels. Atlas labels are overlaid on the DTI OEC maps on the left and the MD maps on the right of each panel. The locations of these axial planes are indicated by the yellow lines on top of a sagittal MD map at the lower left corner.

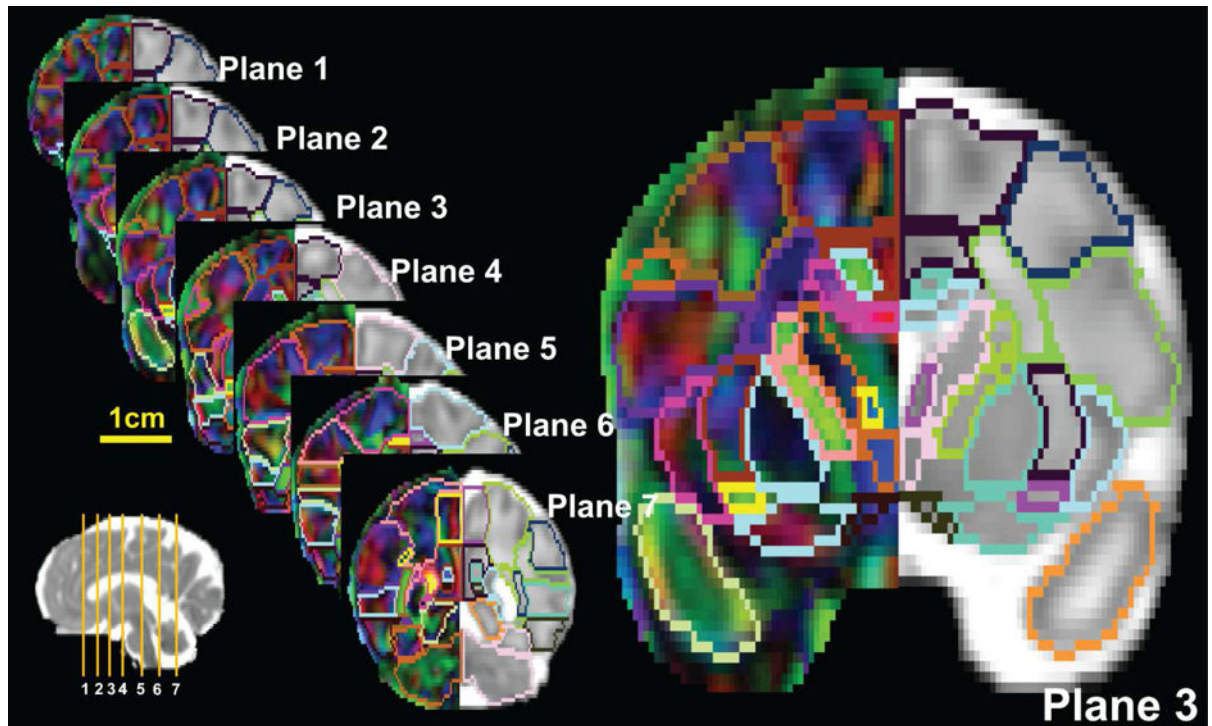


Figure 6.

Coronal planes of the established preterm brain atlas at 33PMW with comprehensive GM and WM labels. Atlas labels are overlaid on the DTI OEC maps on the left and the MD maps on the right of each panel. The locations of these coronal planes are indicated by the yellow lines on top of a sagittal MD map at the lower left corner.

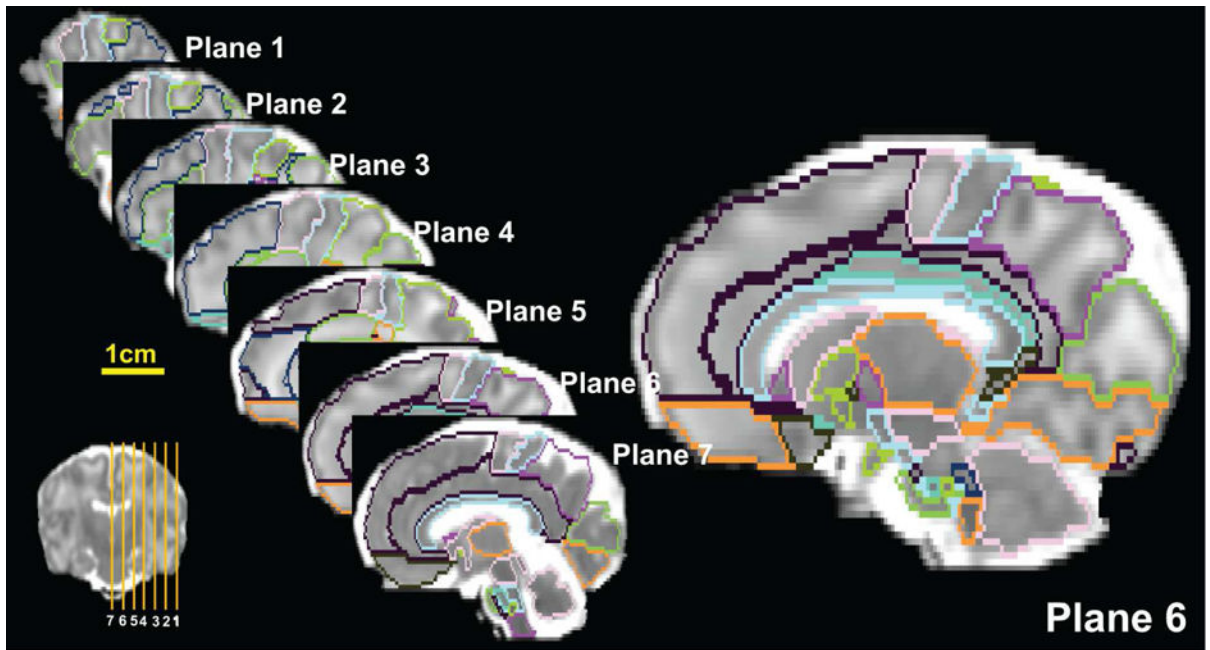


Figure 7. Sagittal planes of the established preterm brain atlas at 33PMW with comprehensive GM and WM labels. Atlas labels are overlaid on the MD maps. The locations of these sagittal planes are indicated by the yellow lines on top of a coronal MD map at the lower left corner.

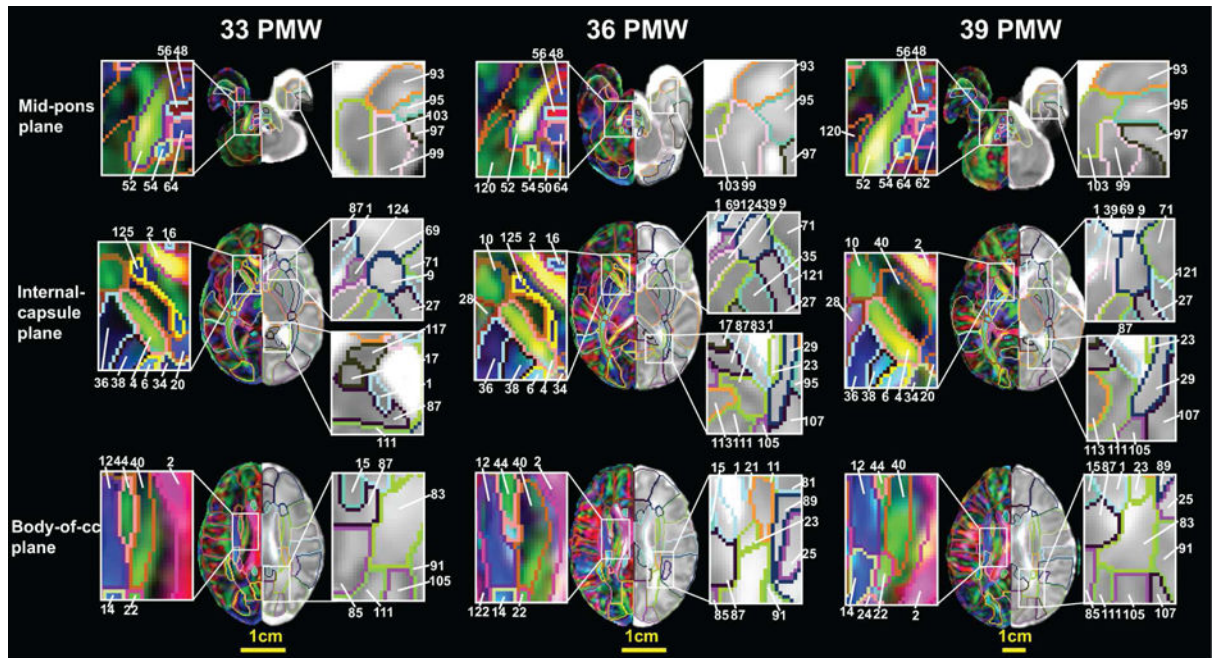


Figure 8.

Axial planes of the age-specific DTI atlases at 33, 36 and 39 PMW with comprehensive GM and WM labels show delineated neural structures with morphologic changes across the postmenstrual ages. The atlas labels are overlaid on the DTI OEC maps (left in the panel) and MD maps (right in the panel). The enlarged regions show the neuroanatomical details of the DTI atlases at the 33, 36 and 39 PMW. The neuroanatomical label indices are listed in the Appendix.

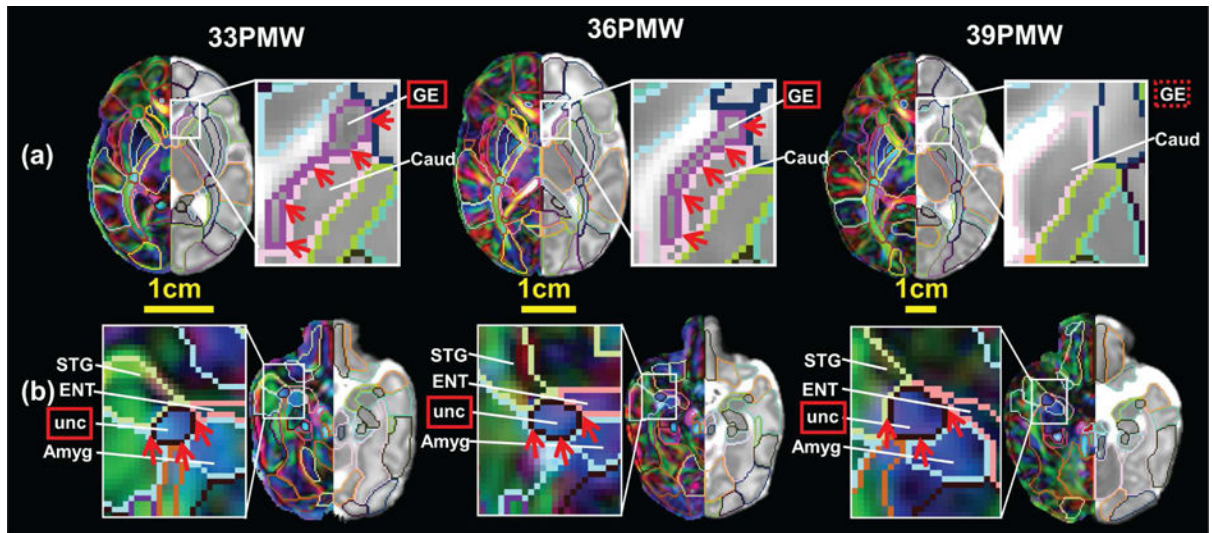


Figure 9: Disappearance of a transient neural structure, ganglionic eminence (GE) and dramatic size increase of uncinatus fasciculus is highlighted in (a) and (b), respectively. These two structures are indicated by red arrows and red boxes. See the table in Appendix for the abbreviation of neural structures.

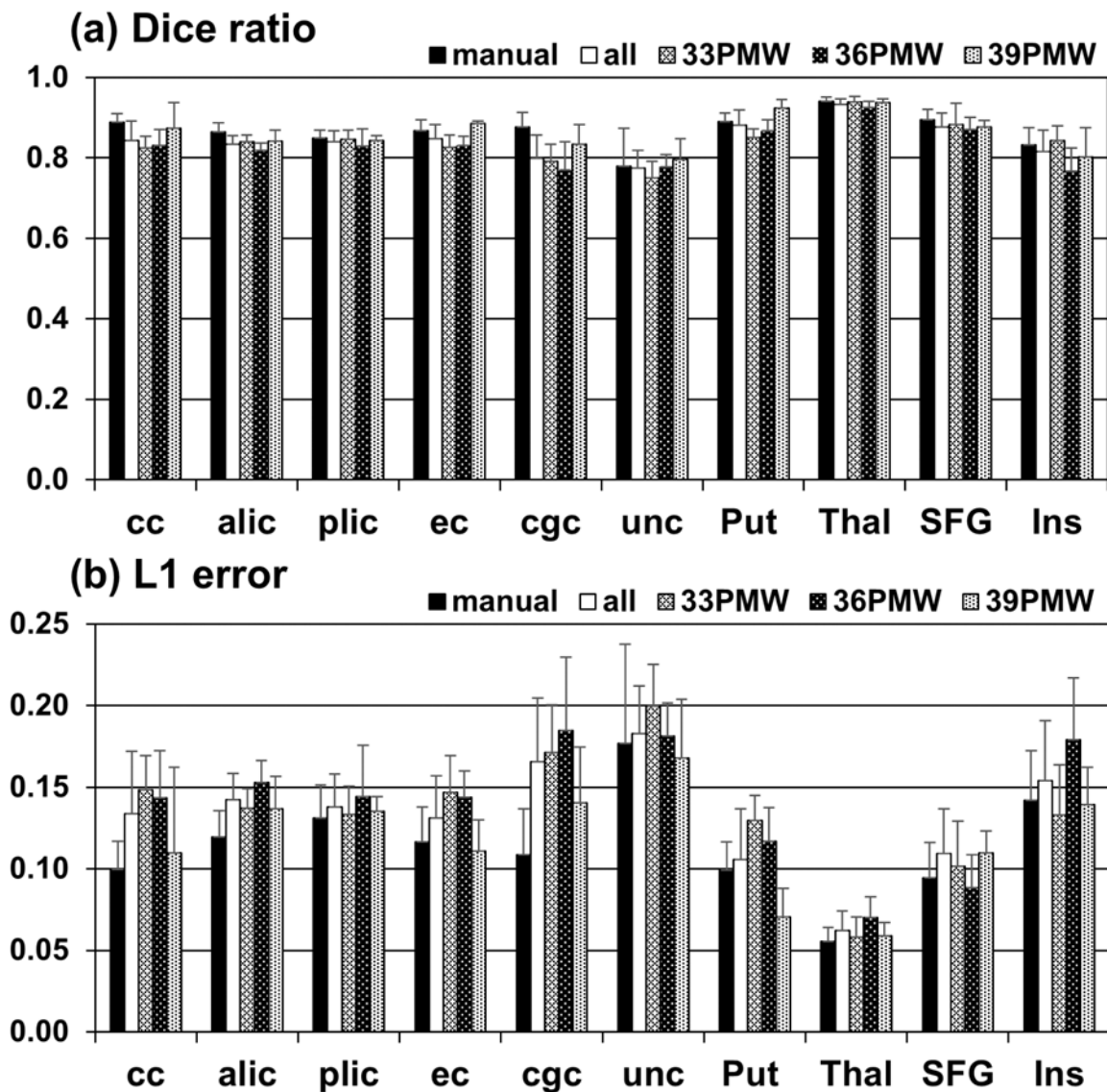


Figure 10:

The Dice ratio (a) and L1 error (b) measurements from the evaluation comparing automated labels with manual labels. The black bars, white bars with crossing lines, black bars with white dots and white bars with black dots in (a) and (b) show the Dice ratio and L1 error measurements based on inter-rater (manual), automated labels of 5 age-matched brains from 33PMW atlas, automated labels of 5 age-matched brains from 36PMW atlas and automated labels of 5 age-matched brains from 39PMW atlas, respectively. The white bars in (a) and (b) shows averaged Dice ratio and L1 error from automated labels of all 15 subject brains. See the table in Appendix for the abbreviation of tested neural structures.

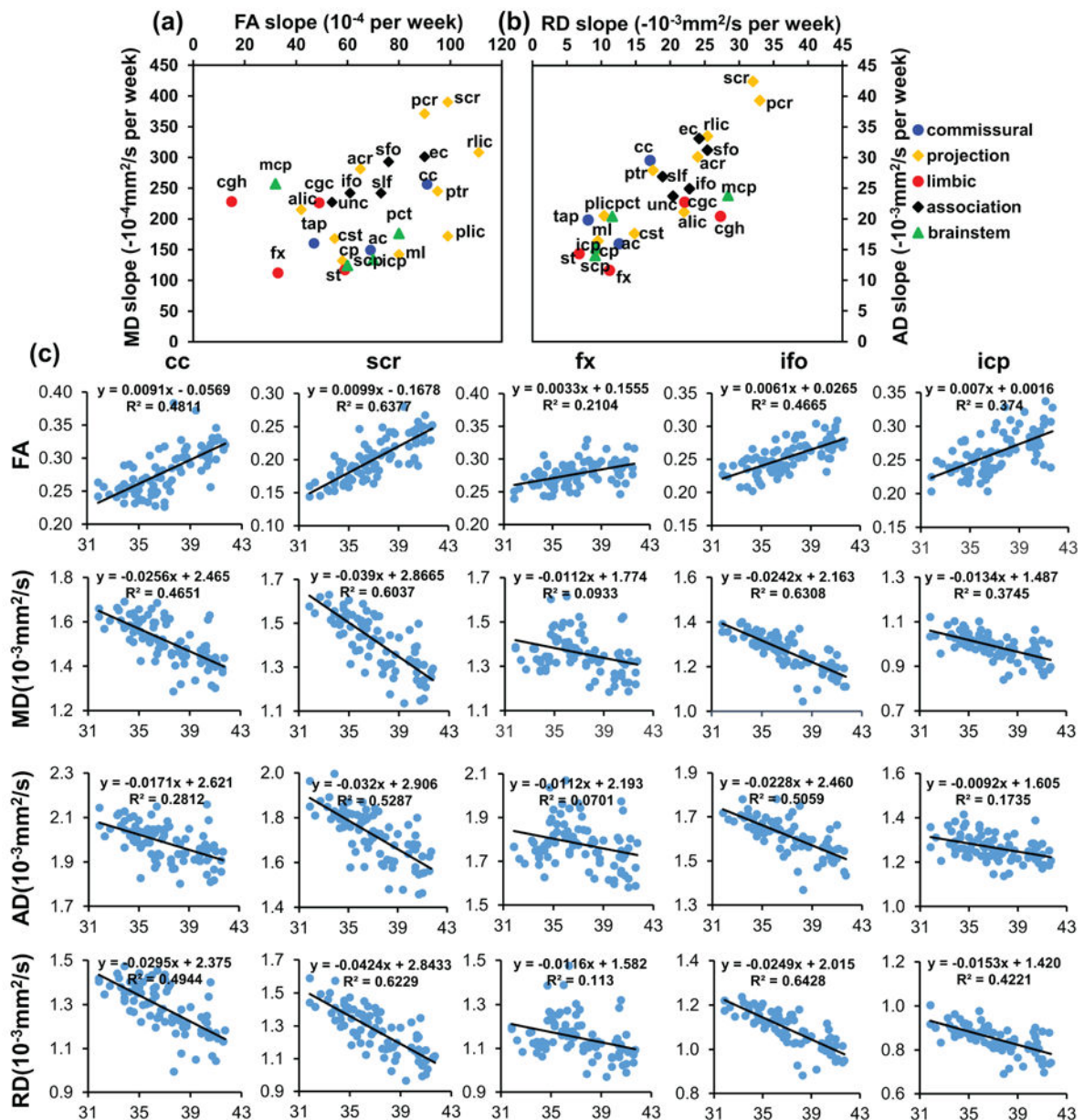


Figure 11:

(a) The relationship between the age-dependent FA increasing slopes and the age-dependent MD decreasing slopes of various WM tracts; (b) The relationship between the age-dependent AD and RD decreasing slopes of various WM tracts. In (a) and (b), the WM tracts are categorized into the commissural (blue dots: ac, cc, and tap), the projection (orange dots: alic, plic, rlic, cp, ptr, acr, scr, and pcr), the limbic (red dots: cgc, cgh, fx, and st), the association (black dots: slf, sfo, ilf, ifo, and unc), and the brainstem (green dots: scp, mcp, icp, and pct) tract group. (c) The scatter plots of age-related FA, MD, AD and RD changes of the five tracts representing the five WM tract groups. See the table in Appendix for the abbreviation of these WM tracts.